Bubble breakup and effects of soluble surfactants on bubble dynamics in a solid-body rotating flow

Majid Rodgar, Hélène Scolan, Jean-Louis Marié, Delphine Doppler, and Jean-Philippe Matas*

Univ Lyon, Ecole Centrale de Lyon, CNRS, Univ Claude Bernard Lyon 1, INSA Lyon, LMFA, UMR5509, 69130, Ecully, France

(Received 30 January 2023; accepted 21 June 2023; published 17 July 2023)

We present experimental results describing the behavior of a bubble placed within a horizontal high-speed solid-body rotating flow. We focus on the stretching and breakup of the bubble that happens in this situation and on the effect that a surfactant introduced in the liquid has on this. In order to explore the effects of surfactants on the bubble we have used two solutions of tetradecyltrimethylammoniumbromide (TTAB), one whose concentration is lower than the critical micelle concentration (0.33 CMC) and one with a concentration larger than the CMC (2 CMC). The results show that, as expected, the deformation of the bubble is larger in both surfactant solutions than in water and can be modeled by the model of Rosenthal 1962 in the case of both solutions. In the case of the 0.33 CMC solution, the bubble behaves as if it were seeing an effective surface tension equal to that in the saturated solution. We observed that the bubble could break up at certain rotational speeds for large bubble sizes. We show that this breakup occurs through a resonance mechanism when the rotational velocity of the tank becomes of the order of the eigenfrequency of the bubble.

DOI: 10.1103/PhysRevFluids.8.073604

I. INTRODUCTION

A. Bubbles in vortices

When a bubble enters a flow with locally high-vorticity regions, it most often remains trapped inside. This is observed in numerous flow situations where these high-vorticity regions exist like mixing layers, turbulence, recirculating flows, and body or propeller wakes [1]. The reason is that the flow inside high-vorticity regions is nonhomogeneous with low-pressure minimums at their center, which induces forces driving bubbles towards the vortex core, as reported in many studies [1–6]. At the laboratory scale, Naciri [7] proposed measurements of these forces in a horizontal solid-body rotating flow, which can be representative of these vortex regions. He found that bubbles released in this type of flow experience, like in shear flows [8–14], a lift force that, adding to the other radial forces (pressure and added mass), make them spiraling towards an equilibrium position located close to the rotation axis, according to the rotation speed. The coordinates of this equilibrium position were used to measure the drag and lift coefficients. Several subsequent studies contributed to determining these forces more precisely, either numerically [15,16] or experimentally [16–20]. All were limited to moderate rotation speeds, a condition for the bubble to be at equilibrium reasonably far from the rotation axis so that it does not disturb the solid-body rotating flow. The property of the interface and its consequences on the bubble dynamics, its deformation, as on its wake were examined considering various cases: clean interface [silicone oils (Rastello *et al.* [19])],

*jean-philippe.matas@univ-lyon1.fr

 ©2023 American Physical Society

interface partially covered with impurities [demineralized water (Rastello *et al.* [18,20], Rastello and Marié [21])], or solid interface [spheres in glycerin mixtures or water (Bluemink *et al.* [15,16])].

B. Bubble behavior in a high-speed solid-body rotational flow

In Rodgar *et al.* [22] we investigated the behavior of a bubble released in a solid-body rotating flow of demineralized water at higher rotation speeds (up to 900 rpm) and for larger bubble diameter than in studies mentioned in the preceding paragraph. At these relatively high velocities, the bubble stabilizes close to the rotation axis, most of the time straddling the axis, thus mimicking the bubbles trapped in a vortex core. We studied the stretching of the bubble as a function of its size and of the rotation of the cell. We showed that the bubble aspect ratio could be well reproduced by the analytical model of Rosenthal [23], provided that the Weber number is corrected to account for the real pressure field seen by the bubble. Indeed, in a horizontal solid-body rotating flow the bubble is slightly shifted from the rotation axis by buoyancy, while the original model assumes an axisymmetry of the bubble around this axis. The drag and lift coefficients were also determined from the bubble position. For large Reynolds numbers, we observed that the bubble became very unstable in position and shape, even leading in some cases to its breakup. The mechanism causing the breakup was suspected to be a resonance.

C. Goal of the present study

Our first objective is to investigate the effect of a surfactant on the bubble stretching and breakup and on the forces acting on the bubble. It has long been known that the presence of contaminants (surfactant or impurities) at the surface could modify the forces acting on the bubble in a spectacular way [20,24,25]. The inclusion of surfactants in the liquid can increase the drag force, hence reducing the bubble rising velocity, and modify the lift force that bubbles experience in shear flows, which may influence their lateral motion in such flows. These changes in behavior are linked to the distribution of surfactant at the surface and the impact this has on the boundary conditions at the interface. This distribution depends on the relative magnitude of the characteristic times of adsorption, desorption, diffusion, and advection of the surfactant at the surface and on the nature of the surfactant as well, solid or soluble [26,27]. For bubbles rising in a quiescent liquid, the contaminants adsorbed are generally convected to the downstream cap of the bubble where they accumulate, thus creating a gradient of surface tension. This gradient generates an interfacial shear stress in the opposite direction, the Marangoni effect [28,29], which slows down the flow at the rear of the bubble and induces an interfacial flow opposing that due to the bubble motion. The consequence is that the upstream cap free from adsorbed contaminant behaves as a mobile surface with vanishing stress, while the downstream cap covered by contaminant is immobile with no slip-condition applying. Small amounts of contaminants may have a significant effect. For example, Lakshmanan and Ehrhard [27] numerically found that surface tension variations of less than 2% could generate Marangoni stresses strong enough to change the rising characteristic of a bubble to that of a solid sphere with the same diameter.

The second objective of the present study is to characterize more precisely the conditions for which bubble breakup happens and confirm that it is actually caused by a resonance phenomenon. As will be presented below, for a given range of rotational velocities, breakup can be observed for a wider range of conditions in the presence of surfactant: The mechanism responsible for bubble instability can then be described more precisely in these conditions than with our previous water experiments [22].

We will introduce the experimental setup in Sec. II, show the results for bubble deformation in the presence of surfactants in Sec. III, and describe breakup conditions in Sec. IV.

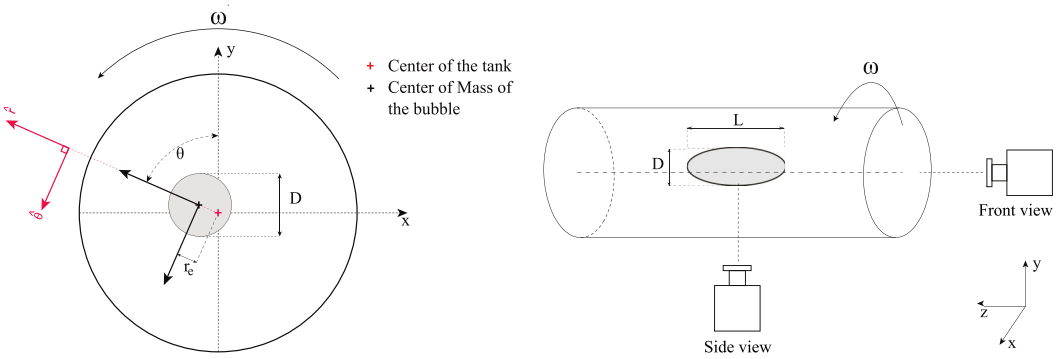

FIG. 1. Left: Configuration of the present problem, showing an approximately axisymmetric bubble close to the axis of rotation z. Right: The experimental setup showing the positioning of the cameras relative to the rotating tank.

II. EXPERIMENT

A. Experimental setup

The experimental setup is shown in Fig. 1 and is identical to the one previously used in Rodgar *et al.* [22]. A Plexiglas tank with a diameter of 11 cm and a length of 10 cm is spun along its horizontal axis z. Three holes on the body of the cylindrical tank are used to either fill in the liquid or inject an air bubble. The range of tank rotation speed ω is [600–900] rpm, i.e., from 63 to 94 rad s^{-1}. Two cameras are used to capture bubble shape and position: a Phantom 4.3 V360 is positioned perpendicular to the axis of rotation (side view in Fig. 1) and records in particular the stretching of the bubble along the axis of rotation. A second camera, Basler acA800, is placed parallel to the cross-section x-y plane, along the axis of rotation (front view in Fig. 1). Two LED panels are used for backlight imaging to facilitate our image processing techniques. The cameras are synced to capture the bubble at the same time at a frame rate of $F = 200$ Hz. The resolution is adjusted at 600×800 pixels for both cameras. For each injected bubble volume and fixed ω, 255 synchronized images are recorded. After suitable calibration accounting for bubble location and refraction due to the cylindrical walls of the tank, the recorded images are processed to extract the contour of the bubble on both side and front views (same setup and method as described in Rodgar *et al.* [22]).

The experiment was performed with water in which a controlled quantity of surfactant is introduced. The water used here is demineralized, similarly to the water used in Rastello *et al.* [18]. Its resistivity is 0.3 MΩ cm. We have used a chemical compound called tetradecyltrimethylammoniumbromide (TTAB), whose molecule is displayed in Fig. 2. The critical micelle concentration (CMC) of TTAB is $C_{\mathrm{CMC}} = 1.5$ g/l. Below the CMC value, we expect the bubble interface to be not entirely saturated. In order to explore the effects of TTAB on bubble dynamics, we have tested two separate TTAB concentrations in demineralized water. One solution of TTAB surfactant lower than C_{CMC} and the other higher than C_{CMC}.

TTAB : tetradecyltrimethylammonium bromide ($C_{14}H_{29}N(CH_3)_3^+ Br^-$)

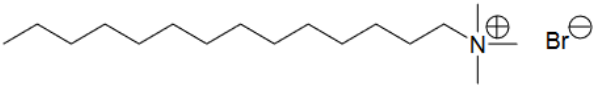

FIG. 2. Structure of the TTAB surfactant molecule. The carbon chain is the hydrophobic side of the surfactant while the N^+ side is the hydrophilic head.

TABLE I. TTAB concentration and surface tension at rest for both solutions used in this study.

Solution name	TTAB concentration (g/l)	Ratio to CMC	Surface tension
C'	0.5	0.33 CMC	$\sigma_{0.33\text{CMC}} = 51.5 \pm 1.0$ mN/m
C''	3	2 CMC	$\sigma_{2\text{CMC}} = 37 \pm 1.0$ mN/m

First, the solution below the CMC condition has been investigated. This solution, which we will call C', has a concentration of 0.5 g/l, corresponding to 0.33 CMC. For the second solution, we chose a concentration of 3 g/l, which is twice the CMC concentration. We call this solution C''. The objective is to test the effect of surfactants for both the unsaturated (lower than CMC, C' solution) and saturated (higher than CMC, C'' solution) interface. A summary of our solutions (C' and C'') concentrations is illustrated in Table I. The surface tension value of each solution, shown in the third column of Table I, has been measured with two different tensiometers. First a pendant drop tensiometer (Attension Theta Flex, Biolin Scientic AB) and a second pendant drop tensiometer (Tracker Standard drop tensiometer). The value of the surface tension measured by both tensiometers are consistent to 1 mN/m.

For performing experiments to analyze the bubble stretching in these two TTAB solutions, we have explicitly chosen bubble volumes that do not lead to rupturing during the experiments. Therefore, in order to understand the dynamics of the bubble in the presence of TTAB surfactant (C' and C'') and compare them with the case of demineralized water, we are limited to a range of volumes not larger than $V = 0.16$ cm^3 for ω in the range [63,94] rad s^{-1} (see Tables II and III).

All the quantities introduced in the following sections related to the bubble size and position are measured for each image and then averaged over the total number of images recorded by each camera. The standard deviation around these averaged values will be indicated by the error bars. We will assume in the modeling that the bubble is axisymmetric, of characteristic lengths L and D (Fig. 1 right). By increasing the rotation speed, the large bubble close to the axis of rotation becomes more axisymmetric, as discussed by Rodgar *et al.* [22] and as will be shown in the following section. For each front view image the equivalent bubble diameter D for a given injected volume and ω is defined as the mean value between minor axis and major axis dimensions, as measured with the Matlab regionprops function. As explained in Rodgar *et al.* [22], the bubble does not strictly converge towards an equilibrium position but rather describes a limit cycle around a given position, as illustrated in Fig. 3 for three different rotation rates. Given that the amplitude of the limit cycle is small compared to the bubble size, in the following we call the "equilibrium position" the mean bubble position. We retrieved the distance of the bubble to the axis of the cell, r_e, by measuring from the images the distance from the center of the cell (using the circular shape of the wall of the tank) to the center of the bubble, output by the regionprops Matlab function which detects the centroid of

TABLE II. Characteristics of the bubbles in solution C' (0.33 CMC): Mean volume V and radius R_{eq} of a spherical bubble of equivalent volume.

Mean volume V (cm^3)	Mean equivalent radius R_{eq} (cm)
0.001	0.072
0.004	0.098
0.013	0.146
0.05	0.228
0.069	0.254
0.078	0.266
0.117	0.303
0.127	0.311

TABLE III. Characteristics of the bubbles in solution C'' (2 CMC): Mean volume V and radius R_{eq} of a spherical bubble of equivalent volume.

Mean volume V (cm^3)	Mean equivalent radius R_{eq} (cm)
0.003	0.09
0.014	0.15
0.025	0.183
0.04	0.21
0.055	0.23
0.083	0.27
0.123	0.308
0.138	0.32
0.141	0.322

the bubble front view projection. The length L is directly measured as the major axis from the side view projection, with the same Matlab function.

B. Dimensionless parameters

We discuss in this section the parameters and corresponding dimensionless numbers needed to describe the position and shape of a bubble of volume V placed in a solid-body rotating flow. As mentioned before we characterize the bubble shape with two lengths: a length L corresponding to the dimension of the bubble along the axis of rotation z and the (supposedly) smaller length scale D, corresponding to the diameter of the bubble projection in a plane normal to the axis of rotation. Two dimensionless numbers are introduced to quantify the shape of the bubble: the aspect ratio $X = L/D$, which determines the stretching of the bubble along the axis, and the aspect ratio X_F, defined as the ratio of major to minor axis as measured on the front view. The physical parameters in this problem are the acceleration of gravity, g; the liquid density, ρ_l; the rotational velocity of the tank, ω; the gas-liquid surface tension, σ; and the dynamic viscosity of the liquid, μ. We add to these quantities the distance of the bubble to the axis of the cell, r_e, which controls the pressure difference seen by the bubble.

We group the above parameters into four independent dimensionless numbers, namely the Rossby number $\mathrm{Ro} = r_e/D$, the Reynolds number $\mathrm{Re} = \rho_l \omega r_e D/\mu$, the Froude number $\mathrm{Fr} = \omega^2 r_e/g$, and the Weber number $\mathrm{We} = \rho_l \omega^2 D^3/8\sigma$. We have chosen here to introduce a Reynolds number based on the mean velocity seen by the bubble. An alternative choice could be to introduce

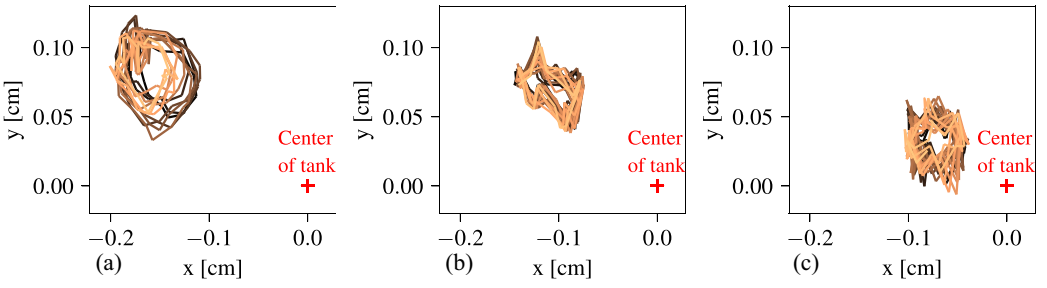

FIG. 3. Limit cycles described by bubble, for C' solution, $V = 0.078$ cm^3 and (a) $\omega = 62.6$ rad s, (b) $\omega = 78.5$ rad s, and (c) $\omega = 94.2$ rad s. The red cross corresponds to the center of the tank.

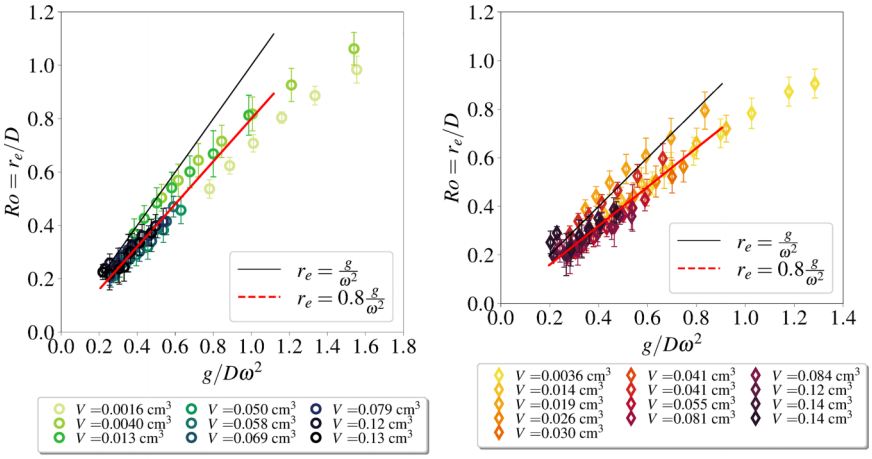

(a) (b)

FIG. 4. Variation of the Rossby number R_o as a function of $g/(D\,\omega^2)$. (a) Bubbles in C' solution. (b) Bubbles in C'' solution. The black line corresponds to $r_e = g/\omega^2$.

a *shear* Reynolds number based on the velocity difference across the bubble:

$$\mathrm{Re}_{\mathrm{shear}} = \frac{\rho_l \omega D^2}{\mu} = \mathrm{Re}/\mathrm{Ro}. \tag{1}$$

As shown in Rodgar *et al.* [22], and as will be detailed in the following section, the main control parameter driving the stretching of the bubble is We, but a correction in Ro has to be introduced.

III. BUBBLE DEFORMATION IN THE PRESENCE OF SURFACTANTS

A. Position of the bubble

We first present measurements of r_e, the distance of the bubble center to the cell axis. We show in Fig. 4 that this distance is approximately proportional to g/ω^2 for both C' and C'' solutions. More precisely, it can be approximated by $r_e = 0.8g/\omega^2$ or equivalently $\mathrm{Ro} \sim 0.8g/D\omega^2$. This behavior has already been observed in experiments carried out without surfactant. It can be understood by considering a simple balance of forces, wherein the dominant forces acting on the bubble are buoyancy and the drag force, which in this regime scales as $\rho_l \omega^2 r_e$ times the volume of the bubble [22].

B. Bubble interface configuration

As already observed in Rodgar *et al.* [22], when the rotation rate is increased, the bubble stretches, as illustrated in Fig. 5 (right column). In order to study the deformation of the bubble in the two different chosen solutions (C' and C''), we first plot the variations of the longitudinal aspect ratio X as a function of the rotational speed. As illustrated in Fig. 6, the aspect ratio X for the case of surfactant solutions is higher than for demineralized water for given volume and ω values. The symbols ◯ (data of C' solution) and ◊ (data of C'' solution) have been shifted up in comparison with symbols × (data of demineralized water) for the same range of volumes ($0.004\ \mathrm{cm}^3 < V < 0.13\ \mathrm{cm}^3$), which shows that the bubble is much more stretched along the horizontal axis in presence of surfactants. This aspect ratio increases when ω is increased, as expected due to the steepening of the centrifugal pressure field around the bubble. Note, however, that a maximum in aspect ratio is observed for larger bubble volumes of both surfactant solutions. A similar maximum had been observed for the larger bubbles investigated in Rodgar *et al.* [22]. This maximum is associated with

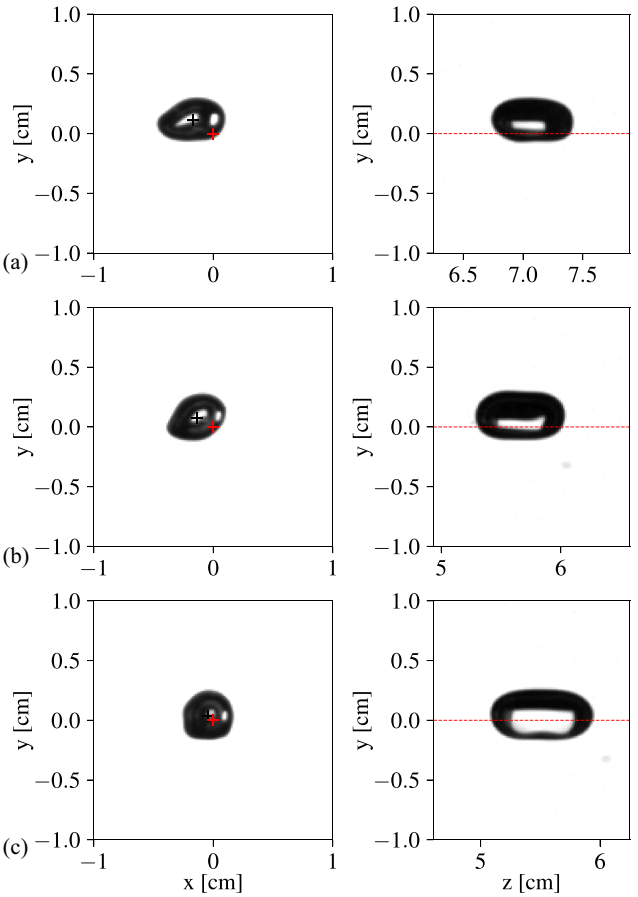

FIG. 5. Instantaneous snapshots of front view (left column) and side view (right column) of the bubble in C' solution for $V = 0.078$ cm^3 and (a) $\omega = 62.6$ rad s, (b) $\omega = 78.5$ rad s, and (c) $\omega = 94.2$ rad s. The red cross corresponds to the center of the tank.

increased fluctuations in bubble shape, and we believe it is related to the nearing of the conditions for breakup (see Sec. IV below).

Since the bubble is close to the axis of rotation, the aspect ratio of the bubble should be predicted by the model of Rosenthal [23], provided the bubble Weber number is replaced by a corrected Weber number We$'$ defined as [22]:

$$\mathrm{We}' = \mathrm{We}(1 + 4\mathrm{Ro}^2), \tag{2}$$

such that the associated We$'$ captures the pressure difference seen by the off-centered bubble and We $= \rho_l \omega^2 D^3/8\sigma$ is the Weber number of the centered bubble defined in Sec. II B. We plot in Fig. 7 the aspect ratio X as a function of this corrected Weber We$'$, taking into account the surface tension values measured by the tensiometers. The data for the C' (0.33 CMC) solution (surface tension lower than CMC) are collapsed but not with the Rosenthal [23] prediction, and the deformation of the bubble is larger than that predicted by the model. However, the data for the C'' (2 CMC) are well fitted with the solid curve of the model (Fig. 7 right), as was the case for demineralized water [22]. Note that the error bars are large for large We: Large fluctuations in aspect ratio are observed when the bubble approaches breakup conditions, see the following section.

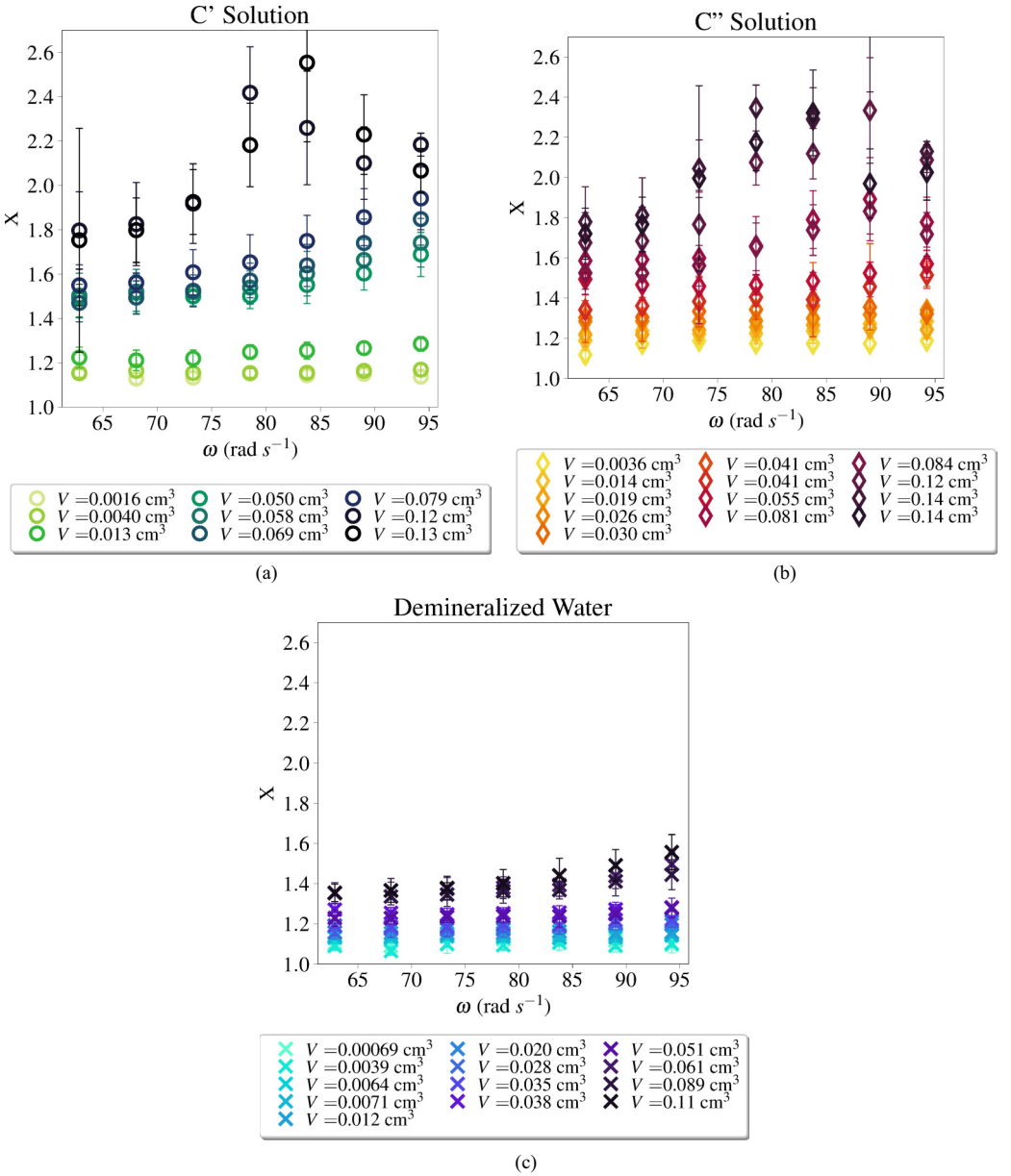

FIG. 6. Aspect ratio of the bubble $X = L/D$ as a function of rotation speed ω (a) for C' solution (0.33 CMC), (b) for C'' solution (2CMC), and (c) for demineralized water; data taken from Ref. [22].

The underprediction of bubble deformation in the C' case suggests that the bubble sees an *effective* surface tension which is different than the surface tension at rest of the C' solution. Figure 8 shows that if the Weber number for this solution is computed with a surface tension of 37 mN/m (which is the CMC value), a good agreement is found with the Rosenthal model. Our interpretation is that in the C' case, there may be an accumulation or inhomogeneous distribution of surfactant on the different regions of the bubble interface, in particular close to the axis of rotation of the tank. This could explain that the effective surface tension seen by the bubble is the CMC concentration even though we are at 0.33 CMC.

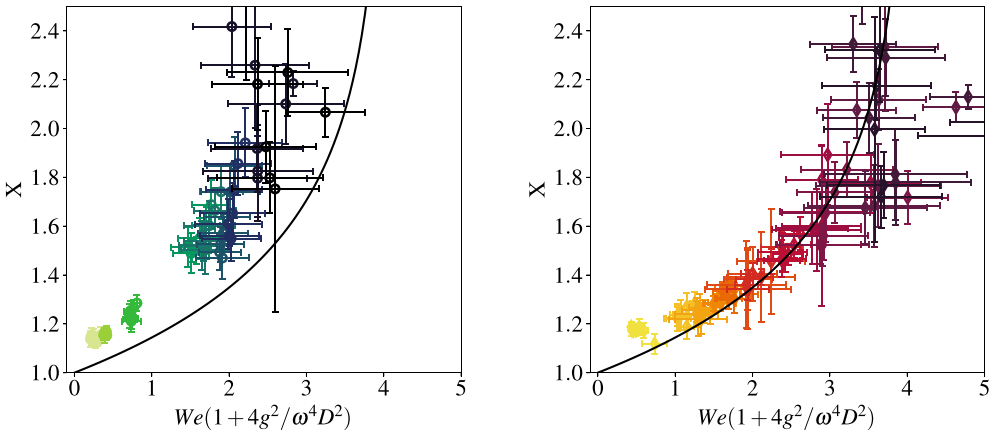

FIG. 7. Bubble aspect ratio $X = L/D$ as a function of corrected Weber number. Left: Bubbles in C' solution. Right: Bubbles in C'' solution. The model works well for the C'' case but underpredicts bubble deformation in the C' case.

More generally, a nonhomogeneous distribution of surfactant is expected to generate Marangoni flow from regions of low surface tension (high concentration in surfactant) to regions of high surface tension (zones depleted in surfactant). Depending on where the surfactant will accumulate, both opposite tendencies can be *a priori* considered: If one assumes that the concentration in surfactant is lower at the tips than at the middle plane, then this will induce a flow towards the tips of the bubble which will enhance the stretching. On the contrary, if the surfactant is mainly accumulated at the tips, then Marangoni stresses will moderate the stretching instead of promoting it. At this stage, we are not able to discriminate between the two hypotheses.

Maps of the average bubble front view contours for three different rotation rates and for the three types of solutions are shown in Fig. 9. While the water and C'' bubbles look very similar for a given ω, the bubble in the C' case exhibits a slightly different orientation. This may be the signature

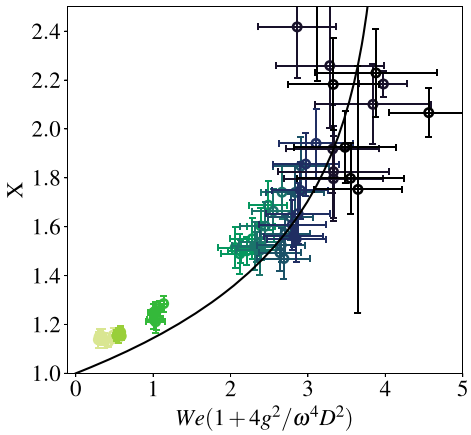

FIG. 8. Bubble aspect ratio $X = L/D$ as a function of the corrected Weber number for the case of the C' solution: When the Weber number is computed with an *effective* surface tension of $\sigma = 37$ mN/m (CMC surface tension), the model is in agreement with the experimental aspect ratio.

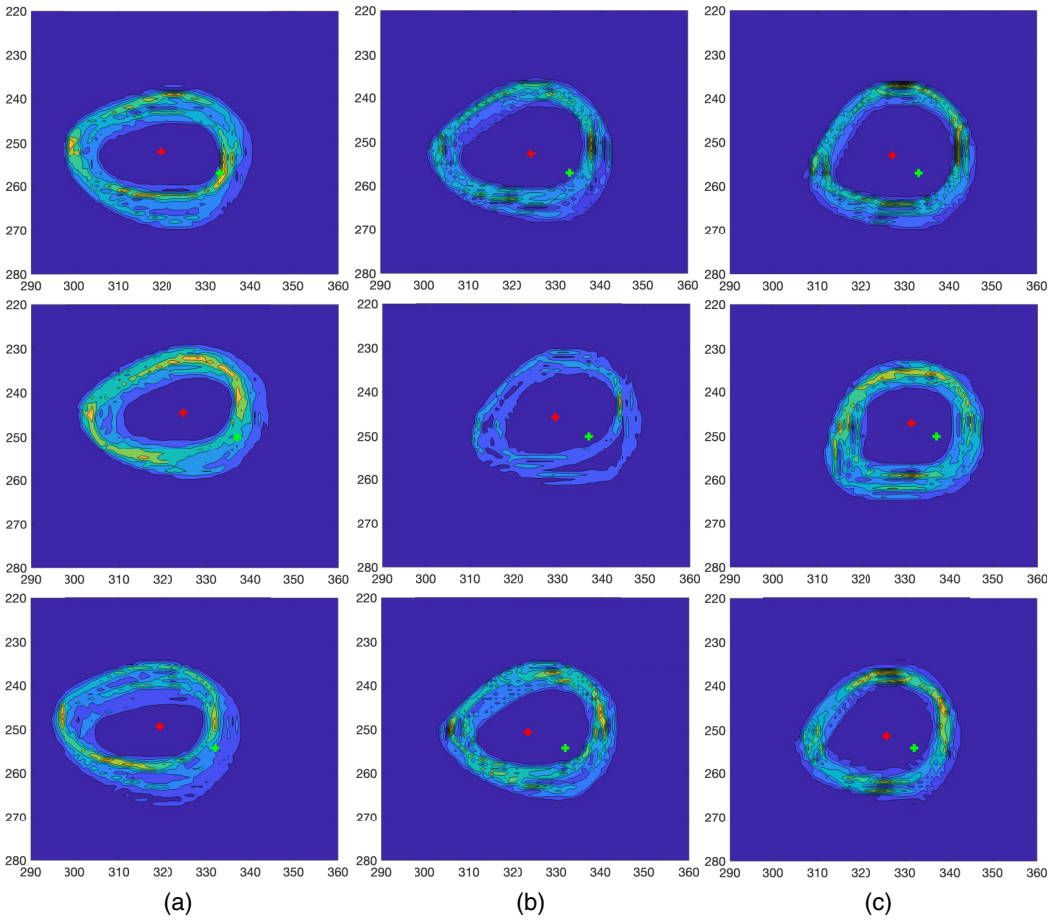

FIG. 9. Average contour of the boundary of the bubble at (a) $\omega = 62.6$ rad s, (b) $\omega = 78.5$ rad s, and (c) $\omega = 94.2$ rad s; first row from top: for water solution $V = 0.06$ cm^3, second row C' solution $V = 0.05$ cm^3, and third row C'' solution $V = 0.05$ cm^3. The red cross corresponds to the associated mean position of the center of the bubble. The green cross corresponds to the center of the tank.

of possible additional Marangoni interfacial flow, due to a nonhomogeneous concentration of the surfactant for this specific case.

The other dimensionless number representing the shape of the bubble is the *front view* aspect ratio X_F, the aspect ratio in the $(\hat{r}, \hat{\theta})$ plane. Figures 5 and 9 illustrate that as ω is increased, the bubble becomes more axisymmetric. This is confirmed in Fig. 10 where X_F decreases with ω except for smaller bubbles for which X_F is already close to 1 for the lowest ω. For both our surfactant solutions the values of the front view aspect ratio (symbols $\diamond$ and $\circ$) are generally slightly higher than that for demineralized water ($\times$) for the same volume range. The values of X_F reach up to 1.6 for C' and C'' but remain close to 1.1 for smaller bubbles (lighter symbols): These bubbles correspond to larger Rossby bubbles which do not straddle the axis of rotation (Ro > 0.5). Note that in spite of relatively large X_F values, the axisymmetry assumption turns out to efficiently capture the stretching of the bubble as predicted by the modified Rosenthal's model once the off-centered bubble position is taken into account (as seen in Fig. 7 for the C'' solution).

The deformation in the cross section is expected to be controlled by the mean velocity seen by the bubble, namely ωr_e. Therefore, the relevant dimensionless number controlling this deformation

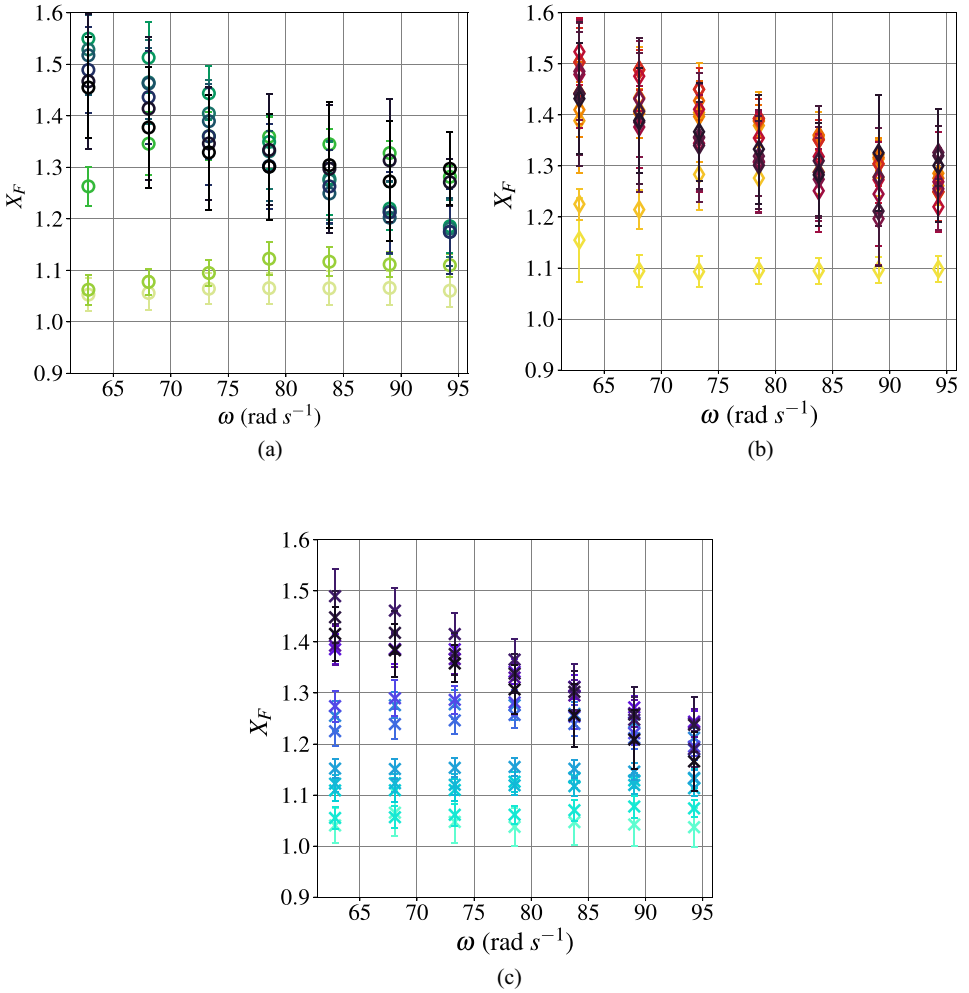

FIG. 10. Variations of the aspect ratio X_F (aspect ratio seen on *front view*) as a function of the rotation speed ω: (a) Bubbles in C' solution (◯), (b) bubbles in C'' solution (◊), and (c) bubbles in demineralized water (×). Same caption as in Fig. 6.

should be the Weber number built with this mean velocity: $\mathrm{We_{re}} = \rho_l (r_e \omega)^2 R/\sigma = 4\mathrm{WeRo}^2$. We test this assumption in Fig. 11, which shows the variations of X_F as a function of $\mathrm{We_{re}}$ for C', C'', and demineralized water data. The figure shows a clear increase of X_F when $\mathrm{We_{re}}$ is increased. The front view aspect ratio for the smaller bubbles (lighter symbols) seems indeed to be controlled by this Weber number. However, for larger bubbles, and larger $\mathrm{We_{re}}$, the data are scattered and do not exhibit the same behavior. This Weber number is expected to be most relevant when the bubble is far from the axis of rotation or at least when it is not straddling it. This condition corresponds to $\mathrm{Ro} > 0.5$. We plot in Fig. 11 (right) the front view aspect ratio of the subset of data for which the $\mathrm{Ro} > 0.5$ condition is fulfilled: As expected, the data are relatively well aligned. Regarding bubbles located closer to the axis of rotation, such that $\mathrm{Ro} < 0.5$, the aspect ratio in the cross section is probably controlled by the wake expected to envelop the bubble for these conditions. The precise description of this dynamics in the very low Ro limit, and its impact on bubble shape, is left for future work.

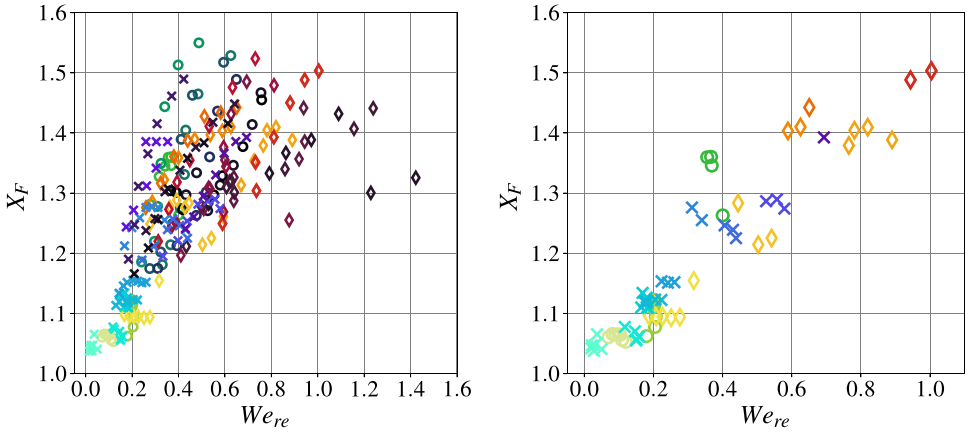

FIG. 11. Left: The front view aspect ratio X_F as a function of $\mathrm{We_{re}}$. ◯, C' solution; ◊, C'' solution; ×, demineralized water. Right: Same plot, only for bubbles such that Ro > 0.5.

IV. BREAK-UP

A. Rupturing without surfactants

As illustrated in the previous section, when ω is increased, the longitudinal aspect ratio of the bubble X increases. This stretching of the bubble can lead to rupturing. We studied this breakup with the following protocol: Starting from rest, the rotation frequency is increased by 5 rad s^{-1} steps, and we wait for 120 s between each step in ω to ensure a stationary regime is reached. The experiment stops when the bubble breaks up. Two different types of breakups have been observed during experiments with this protocol. One is the situation where the bubble splits into two bubbles from the middle. Figure 12 (left) shows the variations of the aspect ratio X of the bubble as a function of time for a bubble of volume $V = 0.3$ cm^3 at $\omega = 89$ rad s^{-1} in demineralized water (without surfactant). After $T = 4.5$ s the bubble becomes distorted and experiences its highest value of X almost up to 5 (twice the average value until $T = 4.5$ s). Rupturing almost simultaneously occurs and the bubble splits into two bubbles of nearly the same size. The sequence associated with this dynamics is illustrated in Fig. 13.

In certain cases, bubble breakup leads to the formation of two bubbles of very different sizes [Figs. 12 (right) and Fig. 14]. When this type of breakup happens, we observe that the longitudinal bubble aspect ratio X increases and reaches a peak, but the bubble does not rupture at this moment:

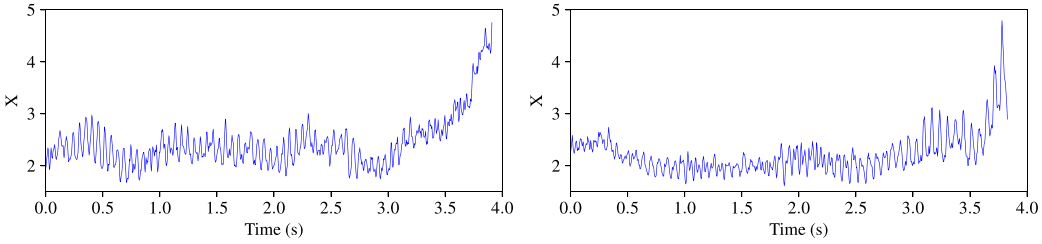

FIG. 12. Bubble aspect ratio X as a function of time. The signal ends when the bubble breaks. Left: Bubble of volume $V = 0.31$ cm^3 at $\omega = 89$ rad s^{-1}. The bubble breaks into two equal size bubbles (corresponding to the sequence of Fig. 13), breakup occurs when maximum aspect ratio is reached. Right: Bubble of volume $V = 0.40$ cm^3 at $\omega = 73$ rad s^{-1}. Breakup does not coincide with the moment of maximum stretching. This results in breakup into two different size bubbles, as illustrated in Fig. 14.

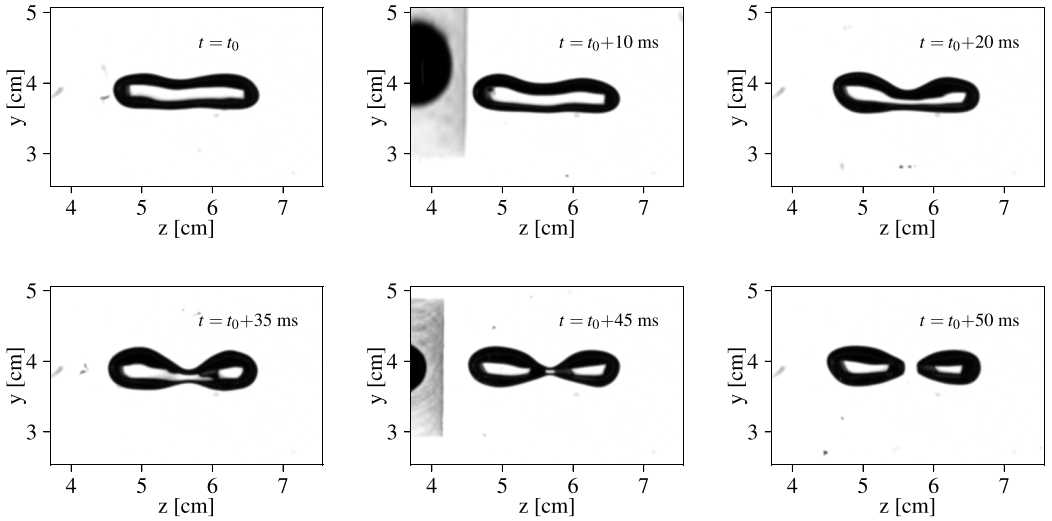

FIG. 13. Example of breakup for a bubble of volume 0.31 cm^3 splitting into two nearly equal size bubbles, at $\omega = 89$ rad s (side view).

Breakup is delayed and occurs at a lower X. This leads to the formation of two dissimilar fragments. Figure 14 illustrates that the decrease of the aspect ratio observed after the peak in aspect ratio, and just before breakup [Fig. 12 (right)], is actually not caused by a longitudinal contraction but by the increase in the cross-sectional size of the bubble just before breakup (images 2 to 5). This could be caused by the drainage of the smaller bubble cavity into the larger cavity, analogously to the emptying of a small bubble into a large one because of Laplace's law. This type of breakup configuration is less frequent than the previous quasisymmetric one. We believe the type of final configuration, with equal or unequal bubbles, is of a stochastic nature and depends on the velocity

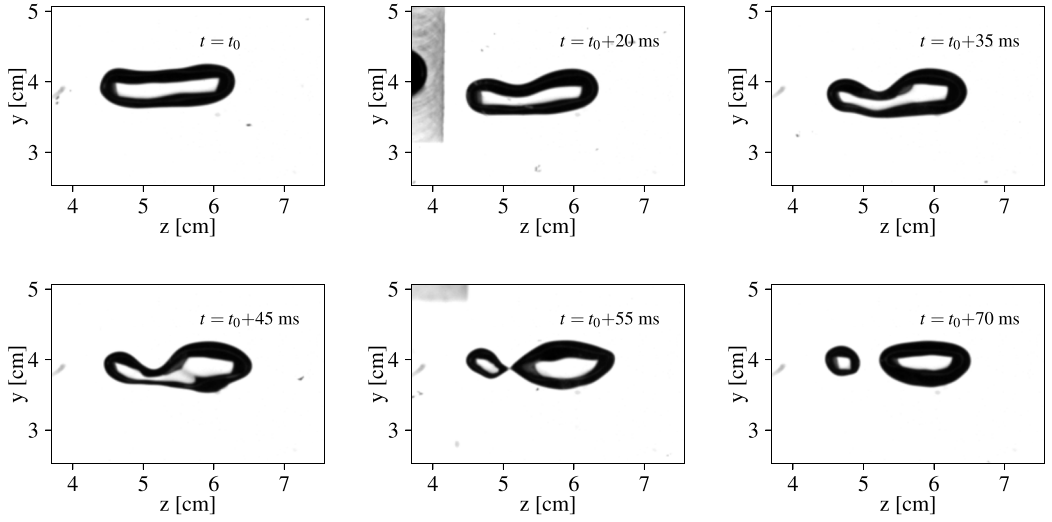

FIG. 14. Example of breakup for a bubble of volume 0.40 cm^3 splitting into a small and a large bubble at $\omega = 73$ rad s (side view).

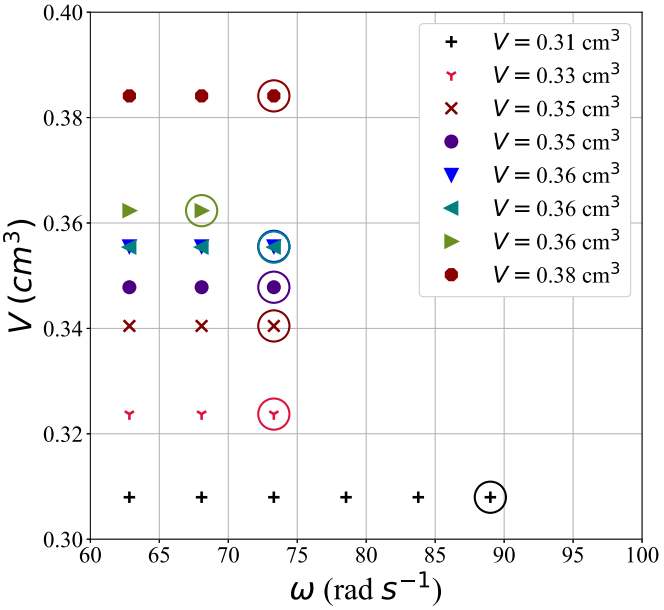

FIG. 15. Volume as a function of ω for the bubbles which experienced breakup. The circles indicate the ω of breakup.

fluctuations in the liquid and on the magnitude of the initial dissymmetry of the bubble when the breakup process is initiated.

Figure 15 illustrates the conditions for which breakup is observed for bubbles in the volume range of [0.31, 0.4] cm^3, when ω is increased step by step. A circle is plotted around the symbol when breakup could be observed. In all the cases of this figure, the bubble breaks *above* a given ω. The smallest bubble which we were able to break ruptured at $\omega \simeq 89$ rad s^{-1}, which is close to the maximum rotation rate our experiment can reach. When bubbles larger than 0.4 cm^3 are injected into the cell, they break during the transient spiraling regime which is observed at startup, and therefore such bubbles cannot be stabilized close to the axis of the cell.

Rosenthal [23] investigated the stability of the bubble to axisymmetric disturbances in his work in order to clarify if the stretching of the bubble could result in a capillary instability as in the classical Rayleigh-Plateau instability [30]. He showed that for large rotation rates, the destabilizing effect of capillarity on the stretched bubble could be balanced by the stabilizing effect of the centrifugal force. More precisely, he proposed a necessary and sufficient condition for stability to such disturbances, in the form:

$$k^2D^2/4 + (\rho_l - \rho_g)D^3\omega^2/8\sigma > 1, \tag{3}$$

where k is the wave number of the considered axisymmetric perturbation, ρ_l the liquid density, and ρ_g the gas density. Note that condition (3) predicts instability *below* a given rotation rate, which is not what we observe experimentally. We plot in Fig. 16 the location of our experimental data points in the $[\omega\sqrt{\frac{D^3(\rho_l-\rho_g)}{8\sigma}}, kD/2]$ plane. We consider perturbations of wave number $k = 4\pi/L$, corresponding to perturbations of wavelength $\lambda = L/2$: All data points fall largely into the stable region, even those for which breakup is observed. Note that given the distance to the instability region, this would also be the case for perturbations such that $\lambda = L$.

As can be seen on the signals of Fig. 12, the uncentered bubble undergoes shape oscillations due to the rotation of the cell and therefore a periodic forcing at ω. The bubble itself has an eigenfrequency which depends on its size. The eigenfrequency of a spherical bubble of radius R

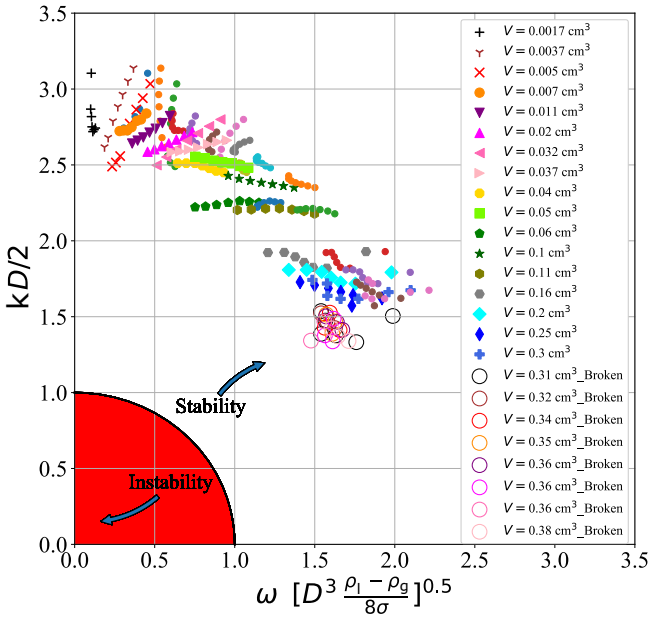

FIG. 16. Stability criterion proposed by Rosenthal [23] in the case of a bubble aligned with the axis of rotation. Here k is the wave number as $2\pi/\lambda$, and λ is the wavelength of the considered perturbation. Experimental data points were plotted for perturbations such that $\lambda = L/2$. All the experimental demineralized water data lie in the stable part of the diagram.

for mode n can be approximated by Rayleigh's formula [31]:

$$\omega_n = \sqrt{\frac{(n-1)(n+1)(n+2)}{\rho_l}\frac{\sigma}{R^3}}. \tag{4}$$

In our case, the bubble is not spherical but elongated: We assume that the above expression can be used to estimate the eigenfrequency with a characteristic size $R \sim L/2$. The frequency of mode $n = 2$ will therefore be

$$\omega_0 = \sqrt{\frac{96}{\rho_l}\frac{\sigma}{L^3}}. \tag{5}$$

This frequency will decrease when ω is increased and the bubble stretches. Figure 17 illustrates the variations of the eigenfrequency of a bubble of volume $V \simeq 0.35$ cm^3 for modes 2, 3, and 4: The eigenfrequency is predicted with the model of Rosenthal [23], which has been shown to predict correctly the stretching of a bubble as a function of ω provided an appropriate correction is included to account for buoyancy [22]. As expected these frequencies decrease as a function of ω when ω is increased, due to the stretching of the bubble. This figure shows that a coincidence of the frequency of the tank (red line) with the frequency of the bubble occurs in the range of investigated rotation rates for modes $n = 2$ and 3. On the other hand, images of the bubble at the moment of breakup (Fig. 13) suggest that the shape mode of the bubble is consistent with mode $n = 2$. Figure 17 shows that the match between cell rotation rate and $n = 2$ eigenfrequency for the $V \simeq 0.35$ cm^3 bubble occurs at $\omega \simeq 66$ rad s^{-1}. Breakup in the experimental data for bubbles of similar volumes is observed between 68 and 73 rad s^{-1}, which is consistent with this value. This suggests that a resonance mechanism is likely responsible for the observed breakup.

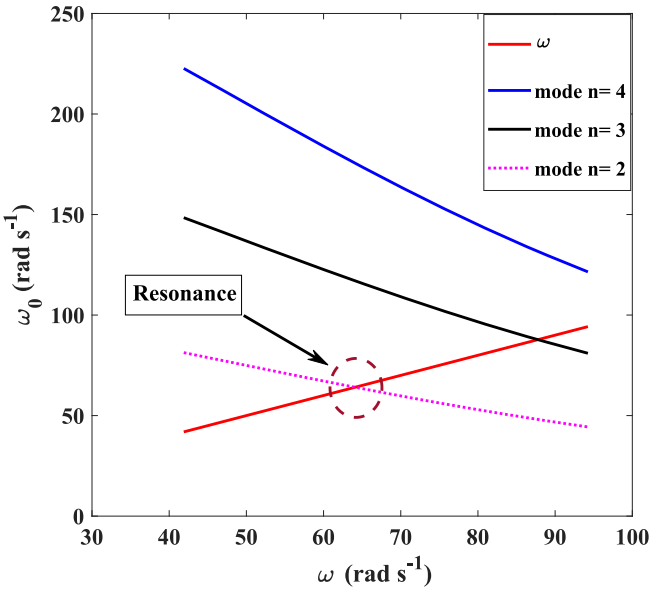

FIG. 17. Predicted eigenfrequencies of a bubble of $V \simeq 0.35$ cm^3 as a function of ω. The red line is the rotational velocity of the tank ω. The dashed magenta curve is the predicted value of the oscillated bubble frequency at shape mode $n = 2$, computed from the model of Rosenthal [23]. Black and blue curves are the calculated frequency of the oscillated bubble in modes $n = 3$ and 4. The circle indicates the moment where the frequency of the bubble coincides with the frequency of the tank at shape mode $n = 2$ ($\omega = 66$ rad s^{-1}).

We plot in Fig. 18 the data of Fig. 15, where we have nondimensionalized ω by ω_{0R} defined as:

$$\omega_{0R} = \sqrt{\frac{12}{\rho_l}\frac{\sigma}{{R_{\text{eq}}}^3}}. \tag{6}$$

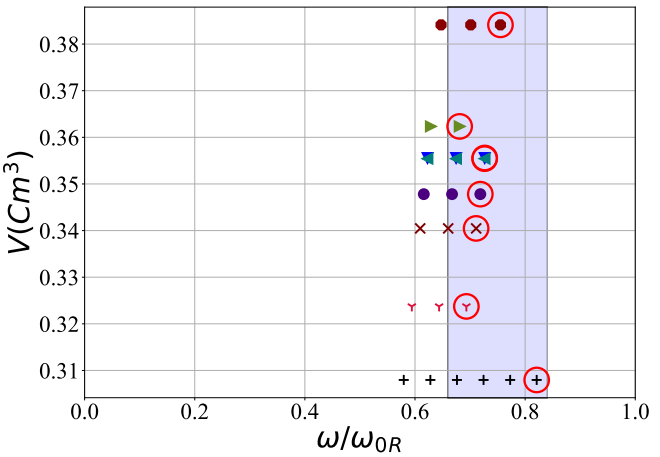

FIG. 18. Volume of the bubble as a function of ratio ω/ω_{0R}, ratio between tank rotation frequency, and eigenfrequency of the equivalent spherical bubble for all experimental series experiencing breakup in water. Circles identify the conditions for which rupturing occurred. Same symbols as in Fig. 15.

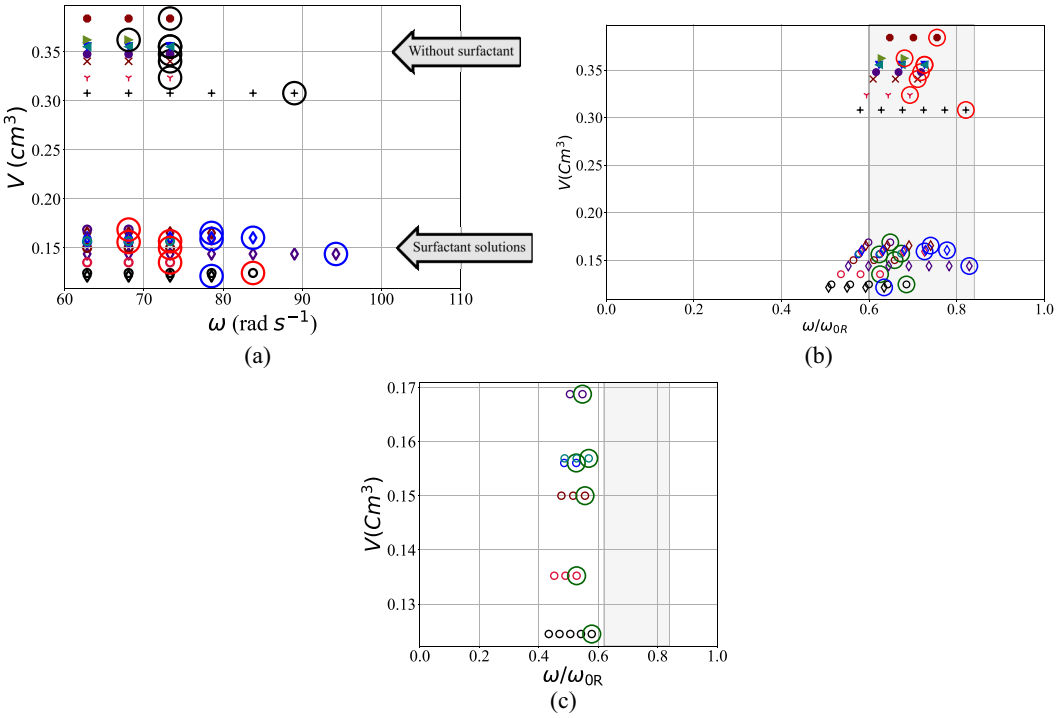

FIG. 19. (a) Experimental conditions of series for which breakup is observed in the (V, ω) plane. Color circles indicate for each series the rotation rate at which breakup occurs (red circles for C' solution; blue circles for C'' solution; black circles for demineralized water). With surfactant (C', ○; C'', ◊) breakup occurs for bubbles with a volume V lower than 0.2 cm^3. Without surfactant (same symbols as in Fig. 15) breakup could only be observed for bubbles with a volume V larger than $V = 0.31$ cm^3. (b) Volume of the broken bubble as a function of ratio ω/ω_{0R} for all experimental series experiencing breakup. (c) Breakup conditions as a function of ω/ω_{0R} fo C' solution, with eigenfrequency computed using surface tension at rest ($\sigma = 52$ mN/m).

In this expression, the eigenfrequency is estimated from the (constant) characteristic size of the bubble R_{eq}, which is the radius of the sphere having the same volume. This reference is chosen, instead of the measured L (bubble major axis) as in Eq. (5), because experimental values of L experience very strong fluctuations close to resonance and because breakup itself tends to introduce a bias towards larger L and hence lower eigenfrequencies. The data of Fig. 18 shows that the values of ω/ω_{0R} for all series are in a range between 0.66 to 0.83. These values are smaller than one: This is consistent with the fact that the eigenfrequency estimated via R_{eq}, which underestimates bubble size, is expected to be larger than the actual bubble eigenfrequency.

B. Rupturing in presence of TTAB surfactant

We now study how breakup of the bubble is impacted by the addition of surfactant to the solution. As for water, we have plotted in Fig. 19(a) the bubble volumes for which rupture is observed and indicated by a color circle the rotation speed ω where breakup occurs for each of these volumes. Results show that bubble breakup occurs in the volume range [0.1, 0.17] cm^3 which is smaller than that without surfactant. This result is expected: Adding surfactant decreases the value of surface tension so that the bubble experiences larger longitudinal stretching and therefore breaks at a smaller volume for a constant ω range.

We have also observed that this breakup occurs like in water, either causing the bubble to break into two fragments of similar sizes or in two markedly unequal sizes following the same scenario

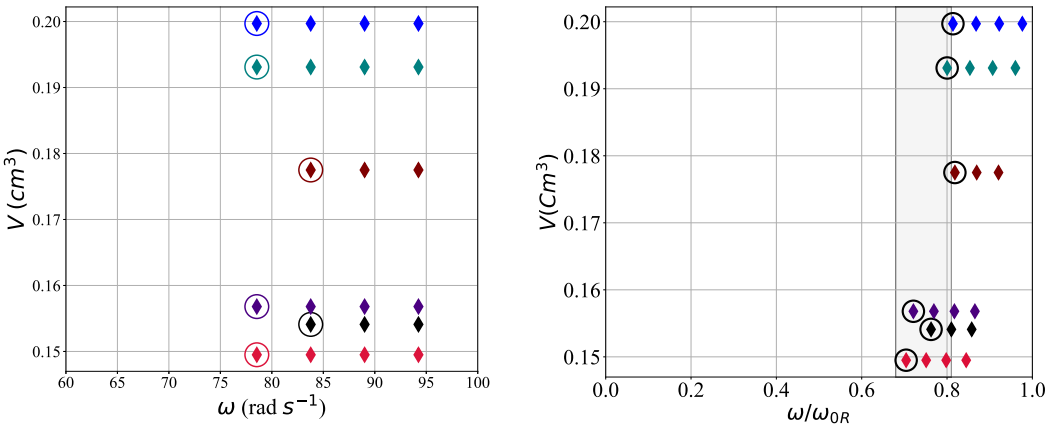

FIG. 20. Left: Volume of the bubble as a function of rotation speed: *reverse* breakup, i.e., breakup obtained by decreasing ω, is observed in C'' (2 CMC) solution. Circles identify the rotation speed ω for which rupturing occurred. Right: Volume of the broken bubble as a function of ratio ω/ω_{0R}.

as that described in Fig. 12. Figure 19(b) shows the values of ω/ω_{0R} when breakup is observed for the various bubble volumes concerned by the rupture. The rupture occurs within a rotational frequency window with ratios located in the range between 0.62 and 0.83. This is similar to what is found in Fig. 18 for water and is thus consistent with the idea that breakup is driven by a resonance mechanism: Bubbles in the presence of surfactant should break when the eigenfrequency of mode 2 of the stretched oscillated bubble is of the same order of magnitude as the rotation tank frequency ω. Note that Fig. 19(b) was obtained with the CMC surface tension for the C' series, 37 mN/n: If, on the contrary, we compute ω_{0R} with the value of surface tension at rest for this solution (i.e., 52 mN/m), then dimensionless frequencies are shifted to lower values, around 0.5; see Fig. 19(c). This suggests, as already mentioned in Sec. III B, that bubbles in this C' solution see an effective surface tension close to the CMC value.

In order to consolidate our assumption that resonance causes breakup, we carried out some additional experiments in which the starting rotation speed is 94 rad s^{-1} and is decreased down to $\omega = 62$ rad s^{-1}. This *reverse* breakup experiment has been performed for the C'' (2 CMC) solution in a range of volumes $V = [0.14, 0.21]\,cm^3$ (the same range of volume for which the breakup occurred by increasing ω in the previous experiments). Note that in order to reach the rotation speed of 94 rad s^{-1} without breaking the bubble, we proceed differently than for the experiments of Figs. 18 and 19: Rotation frequency is increased by larger steps of 20 rad s^{-1} instead of 5 rad s^{-1}, and instead of waiting for 120 s between each increase, we only wait for a maximum of 10 s. The flow regime around the bubble is therefore *a priori* always in a transient regime before reaching the aimed rotation frequency of 94 rad s^{-1}. The aim of this technique is to reach 94 rad s^{-1} without breaking the bubble. Once this frequency is reached, we start measurements: We decrease frequency with smaller 5 rad s^{-1} steps and wait for 120 s between each step, symmetrically to what has been done for the data of Fig. 19.

Figure 20 represents the bubble breakup when we reversely vary the rotational velocity of the tank. Circles indicate the conditions for which breakup occurred. We see the breakup of the bubbles with similar volume sizes as the bubbles in previous experiments of increasing ω but this time happening *below* a given rotational velocities. The values of the ratio ω/ω_{0R} are plotted in Fig. 20 (right): They are between 0.62 and 0.83, which is consistent with our previous experiments (gray zone in Fig. 19 right) and corresponds to the same dimensionless frequency window as in the experiments in Fig. 18. This is another indicator that resonance is the likely reason for bubble breakup in this flow situation.

V. CONCLUSION

We have investigated in this study the behavior of a bubble in a horizontal high-speed solid-body rotating flow with a soluble surfactant (TTAB). We discussed the bubble shape, position, and the nature of the mechanism responsible for bubble rupture. We have compared the behavior of the bubble in two different TTAB solutions: one with a concentration below the CMC (0.33 CMC) and the other one at twice the CMC concentration. Results were compared with those obtained with demineralized water [22].

In the same range of volume sizes, we found that the longitudinal aspect ratio of the bubble in both TTAB solutions is higher than in the demineralized water case, with a bubble more stretched along the axis of rotation. We found a good agreement between the experimentally measured aspect ratio and the prediction of our model based on the Rosenthal [23] prediction for the 2 CMC case when the interface is saturated. However, the model underpredicts the experimental results for the 0.33 CMC solution (wherein the interface is not entirely saturated). We observe that in this case, the bubble stretches as if the surface tension was that of the CMC, i.e., lower than the surface tension measured for this solution at rest: This behavior is probably caused by a nonuniform distribution of surfactant around the bubble.

Finally, we discussed in Sec. IV the conditions for which breakup of the bubble could be observed. When the flow rotation frequency is increased this breakup occurs above a given frequency. In surfactant solutions, it can be observed for smaller bubble volumes than in water for the same range of ω. We showed that the rotation rates for which breakup is observed coincide with an estimate of the eigenfrequency of the bubble ω_{0R}. Moreover, we presented a series of experiments in which we were able to jump above resonance and breakup the bubble by *decreasing* the rotation frequency. The values of ω/ω_{0R} at breakup for this series are in the same range as for the previous series for which ω was increased. This is a strong argument in favor of a resonance mechanism.

The dimensionless parameter controlling this resonance is ω/ω_{0R}: Even though this parameter is not explicitly mentioned in Sec. II B addressing the dimensional analysis of this problem, it can actually be directly related to the Weber number of the bubble as $\omega/\omega_{0R} = \sqrt{2\mathrm{We}/3}(R_{\mathrm{eq}}/D)^{3/2}$. The question of the effective surface tension value seen by the bubble when the interface is not saturated with surfactants, and hence of its effective Weber number, is a crucial issue to determine bubble shape and stability: Numerical simulations in which surfactant exchange between interface and bulk is modeled [32] could yield insight into the surfactant distribution around the bubble and in its wake.

ACKNOWLEDGMENTS

We thank Marie Le Merrer for her suggestions regarding the use of TTAB. This research was supported by the French Agence Nationale de la Recherche ANR under Grant No. SURFBREAK ANR-18-CE08-0013.

[1] S. Green, *Fluid Vortices* (Springer Science + Business Media, Dordrecht, 1995).

[2] G. Sridhar and J. Katz, Drag and lift forces on microscopic bubbles entrained by a vortex, Phys. Fluids **7**, 389 (1995).

[3] M. Marten, K. Shariff, S. Psarakos, and D. White, Ring bubbles of dolphins, Sci. Am. **275**, 82 (1996).

[4] J. Choi and G. L. Chahine, Non-spherical bubble behavior in vortex flow fields, Comput. Mech. **32**, 281 (2003).

[5] N. Jha and R. Govardhan, Interaction of a vortex ring with a single bubble: Bubble and vorticity dynamics, J. Fluid Mech. **773**, 460 (2015).

[6] D. Cabut, M. Michard, S. Simoens, L. Méès, V. Todoroff, C. Hermange, and Y. L. Chenadec, Analysis of the water flow inside tire grooves of a rolling car using refraction particle image velocimetry, Phys. Fluids **33**, 032101 (2021).
[7] A. Naciri, Contribution à l'étude des forces exercées par un liquide sur une bulle de gaz: Portance, masse ajoutée et interactions hydrodynamiques, Ph.D. thesis, Ecole Centrale de Lyon, 1992.
[8] P. Saffman, The lift force on a small sphere in a slow shear flow, J. Fluid Mech. **22**, 385 (1965).
[9] T. Auton, The lift force on a spherical body in a rotational flow, J. Fluid Mech. **183**, 199 (1987).
[10] E. Ervin and G. Tryggvason, The rise of bubbles in a vertical shear flow, J. Fluid Eng. **119**, 443 (1997).
[11] J. Magnaudet and D. Legendre, Some aspects of the lift force on a spherical bubble, Appl. Sci. Res. **58**, 441 (1998).
[12] A. Tomiyama, H. Tamai, I. Zun, and S. Hosokawa, Transverse migration of single bubbles in simple shear flows, Chem. Eng. Sci. **57**, 1849 (2002).
[13] F. Takemura, J. Magnaudet, and P. Dimitrakopoulos, Migration and deformation of bubbles rising in a wall-bounded shear flow at finite reynolds number, J. Fluid Mech. **634**, 463 (2009).
[14] K. Hayashi, D. Legendre, and A. Tomiyama, Lift coefficients of clean ellipsoidal bubbles in linear shear flows, Int. J. Multiphase Flow **129**, 103350 (2020).
[15] J. Bluemink, D. Lohse, A. Prosperetti, and L. V. Wijngaarden, A sphere in a uniformly rotating or shearing flow, J. Fluid Mech. **600**, 201 (2008).
[16] J. Bluemink, D. Lohse, A. Prosperetti, and L. V. Wijngaarden, Drag and lift forces on particles in a rotating flow, J. Fluid Mech. **643**, 1 (2010).
[17] E. A. Van nierop, S. Luther, J. Bluemink, J. Magnaudet, A. Prosperetti, and D. Lohse, Drag and lift forces on bubbles in a rotating flow, J. Fluid Mech. **571**, 439 (2007).
[18] M. Rastello, J. Marié, N. Grosjean, and M. Lance, Drag and lift forces on interface-contaminated bubbles spinning in a rotating flow, J. Fluid Mech. **624**, 159 (2009).
[19] M. Rastello, J. Marié, and M. Lance, Drag and lift forces on clean spherical and ellipsoidal bubbles in a solid-body rotating flow, J. Fluid Mech. **682**, 434 (2011).
[20] M. Rastello, J. Marié, and M. Lance, Clean versus contaminated bubbles in a solid-body rotating flow, J. Fluid Mech. **831**, 592 (2017).
[21] M. Rastello and J. Marié, Wake behind contaminated bubbles in a solid-body rotating flow, J. Fluid Mech. **884**, A17 (2020).
[22] M. Rodgar, H. Scolan, J.-L. Marié, D. Doppler, and J.-P. Matas, Bubble behaviour in a horizontal high-speed solid-body rotating flow, J. Fluid Mech. **925**, A34 (2021).
[23] D. Rosenthal, The shape and stability of a bubble at the axis of a rotating liquid, J. Fluid Mech. **12**, 358 (1962).
[24] R. Clift, J. Grace, and M. Weber, *Bubbles, Drops and Particles* (Academic Press, New York, 1978).
[25] S. Tagaki and Y. Matsumoto, Surfactant effect on bubble motion and bubbly flows, Annu. Rev. Fluid Mech. **43**, 615 (2011).
[26] B. Cuenot, J. Magnaudet, and B. Spennato, The effects of slightly soluble surfactants on the flow around a spherical bubble, J. Fluid Mech. **339**, 25 (1997).
[27] P. Lakshmanan and P. Ehrhard, Marangoni effects caused by contaminants adsorbed on bubble surfaces, J. Fluid Mech. **647**, 143 (2010).
[28] A. Frumkin and V. G. Levich, On surfactants and interfacial motion, Zh. Fiz. Khim. **21**, 1183 (1947).
[29] V. Levich, *Physicochemical Hydrodynamics* (Prentice Hall, Hoboken, NJ, 1962).
[30] L. Rayleigh, On the instability of a cylinder of viscous liquid under capillary force, Phil. Mag. **34**, 145 (1892).
[31] A. Prosperetti, Free oscillations of drops and bubbles: The initial-value problem, J. Fluid Mech. **100**, 333 (1980).
[32] A. Titta, M. L. Merrer, F. Detcheverry, P. Spelt, and A.-L. Biance, Level-set simulations of a 2d topological rearrangement in a bubble assembly: Effects of surfactant properties, J. Fluid Mech. **838**, 222 (2018).